He atom scattering and theoretical study of the surface phonons of a simple benchmark system: Xe(111)

Antonio Šiber and Branko Gumhalter*
Institute of Physics of the University, P.O. Box 304, 10001 Zagreb, Croatia

Andrew P. Graham† and J. Peter Toennies
M. P. I. für Strömungsforschung, Bunsenstraße 10, D-37073 Göttingen, Germany
(Received 26 July 2000; revised manuscript received 9 October 2000; published 28 February 2001)

Low-energy inelastic helium atom scattering measurements of the Xe(111) surface phonon dispersion curves are presented and compared with the results of extensive lattice dynamics analysis and complete one-phonon and multiphonon scattering calculations in the exponentiated distorted-wave Born approximation. The comparisons show that the Xe(111) surface phonon dispersion curves and the individual excitation time-of-flight peak intensities are well described using the gas-phase He-Xe and Xe-Xe pair potentials.

DOI: 10.1103/PhysRevB.63.115411 PACS number(s): 68.35.Ja, 34.50.Dy, 63.22.+m

I. INTRODUCTION

The surfaces of the rare gas solids and their thin films are considered to be ideal model systems for the investigation of interlayer and intralayer interactions since the two body forces between the rare gas atoms are well known.[1] Consequently, the structure and dynamics of the rare gas monolayer and bulk solid surfaces have been studied extensively using inelastic neutron scattering (INS),[2] helium atom scattering[3–8] (HAS), low-energy electron diffraction[9,10] (LEED), ultraviolet photoemission spectroscopy[11–18] (UPS), angle resolved ultraviolet photoelectron emission spectroscopy[19–21] (ARUPS), inverse photoemission spectroscopy[22,23] (IPES), thermal desorption spectroscopy[24] (TDS), scanning tunneling microscopy[25] (STM), and scanning force tunneling microscopy[26] (SFM). The large body of information made available from these studies has also provided important information on the interactions among noble gas atoms in the condensed phase.

Of particular interest in recent years has been the first observation of low-frequency dispersive modes in xenon monolayers on several different metal substrates using low-energy HAS, in addition to the intense and nearly dispersionless, perpendicularly polarized *S* modes.[27–33] These dispersive modes were initially interpreted as being due to the kinematically allowed excitation of the longitudinal acoustic (L) phonon branch in the sagittal plane. However, in the case of Xe monolayers on Cu(001),[30] Cu(111),[31,32] and NaCl(001) (Ref. 33) substrates this interpretation required a decrease of the values of the intraplanar Xe-Xe force constants by a factor of 4 relative to those obtained from the gas phase potentials. The excitation of the shear horizontal (SH) phonon modes was initially ruled out due to their nearly orthogonal polarization with respect to the sagittal plane in which the beam scattering experiments were carried out.[32] At about the same time it was pointed out that the SH-mode dispersion curve calculated from the Xe-Xe gas phase potentials provided a good fit to the new dispersive mode in the system Xe/Cu(001).[34] This controversy has recently been resolved by a detailed study of the phonons of argon, krypton, and xenon monolayers on Pt(111) where all three phonon branches were found for the first time, so that the assignment of the new mode as being SH is now assured for these three monolayer systems.[35] This study showed, further, that the SH mode is only observable for low incident He atom energies of about 8–10 meV. This still leaves open the question as to the actual mechanism by which the SH mode is excited in the sagittal-plane scattering geometry.

To shed more light on this problem, new HAS measurements of the phonon dynamics of the (111) surface of a multilayer solid consisting of approximately 160 layers of Xe atoms on Pt(111) were undertaken for incident energies in the same low-energy range as for the monolayer solids. Since the Xe-Xe gas phase potential has been well characterized,[36] and the Xe bulk phonons extensively studied,[37] the Xe surface provides an important benchmark model system. Moreover, because the local environment of the uppermost xenon layer is quite different from that of the monolayer-metal substrate, the results should serve to reduce the number of possible explanations for the anomalous excitation of the SH mode in the monolayer films. Previously, the Xe(111) surface had been extensively studied by HAS (Refs. 3–8) but only for higher incident energies, above 18 meV. Those studies provided detailed information on the surface Rayleigh phonon branches but, unfortunately, no signatures of either the shear horizontal or the longitudinal modes were found. The present HAS study presents evidence for both of these additional dispersive modes as well as of additional multiphonon effects which may show up already at low He atom incident energies. These results are interpreted with the aid of lattice dynamical analyses in combination with simulations of the HAS time-of-flight (TOF) inelastic scattering intensities based on complete one-phonon and multiphonon calculations in the exponentiated distorted-wave Born approximation, encompassing also the evaluation of the relevant phonon-induced Debye-Waller factors. The good agreement with the experimental results demonstrates that the dispersive phonon branches can be correctly modeled using unperturbed gas-phase potentials, as found previously for the Rayleigh mode.[5] In addition, no anomalous intensity behavior is evident, indicating that the earlier ob-

servation of the SH modes in the rare gas monolayers is probably related to the interaction with the metal substrate, possibly through the surface corrugation.[35]

This paper is organized as follows. In the next section the experimental details will be presented, followed by the HAS results in Sec. III. The Born–von Kármán analysis of Xe(111) phonons is presented in Sec. IV. The theoretical model of inelastic atom-surface scattering is presented in Sec. V and discussed in Sec. VI in comparison with the experimental results. The main conclusions are summarized in Sec. VII.

II. EXPERIMENTAL

The high-resolution helium atom surface scattering apparatus[38] (HUGO II) incorporates a variable temperature ($T_0=20$–400 K) supersonic helium atom beam source with a typical velocity full width at half maximum of $\Delta v/v \simeq 1\%$. The scattered helium atoms are detected at a fixed total scattering angle of $\theta_{SD}=95.8°$ with respect to the incoming beam by a homemade electron bombardment mass-spectrometer detector mounted 1.4 m from the target. A wide range of parallel momentum transfer is accessed according to

$$\Delta K = k_f \sin(\theta_{SD} - \theta_i) - k_i \sin(\theta_i), \tag{1}$$

where k_i and k_f are the incident and final momenta of the helium atoms in the sagittal plane, respectively. Time-of-flight (TOF) measurements, with an energy transfer resolution of typically $\delta(\Delta E) \simeq 0.2$ meV, were made by pulsing the helium beam using a mechanical chopper mounted before the sample, and measuring the flight times of helium atoms to the detector.

The xenon crystal was grown *in situ* by exposing a Pt(111) surface to xenon gas from a 60 cm distant differentially pumped effusive source directed normal to the surface. The mechanically polished Pt(111) single crystal surface was first aligned to within 0.2° and mechanically polished before being inserted into the vacuum chamber where it was cleaned *in situ* in vacuum with repeated cycles of argon ion sputtering ($1\ \mu A\,cm^{-2}$ at 900 eV) and annealing at $T_s = 1200$ K until no contamination could be detected with Auger spectroscopy and the helium scattering diffraction pattern showed a smooth surface with a low concentration of defects. The target chamber, in which the platinum sample was mounted, was kept at a base pressure of $<5\times10^{-11}$ mbar to maintain sample cleanliness during the experiments. The surface temperature was controlled using a Ni-CrNi thermocouple clamped to the side of the sample with an absolute accuracy of $\Delta T_s \sim \pm 5$ K.

III. RESULTS

Figure 1 shows the variation of the surface reflectivity obtained by measuring the helium specular peak intensity as the Pt(111) surface is exposed to xenon at a constant rate. Since the surface temperature of $T_s=50$ K during growth is lower than the multilayer desorption temperature of $T_s \approx 55$ K, a thick Xe layer is expected. The specular reflectivity decreases sharply to a minimum after 50 sec before rising to a small maximum at 60 sec, indicating the formation of an ordered monolayer. Exposure was continued until an estimated 160 monolayers had been adsorbed assuming layer-by-layer growth with a constant sticking coefficient. The continuing downward intensity is attributed to the cumulative build up of defects in or on the xenon layers.

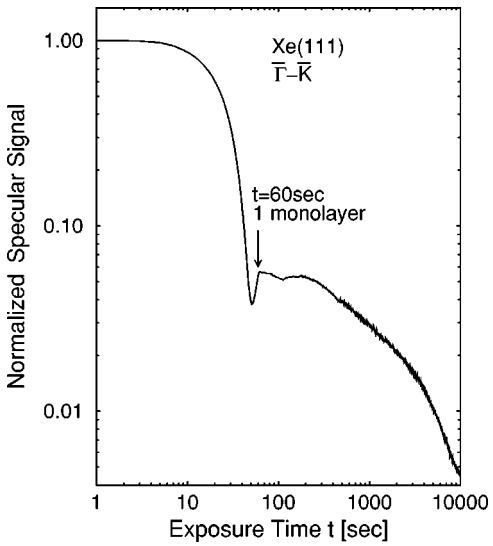

FIG. 1. Dependence of the helium specular signal measured along the Pt(111) $[11\bar{2}]$ azimuth, normalized to the Pt(111) clean surface, during xenon exposure at $T_s=50$ K and an incident helium atom beam energy $E_i=5.3$ meV. The maximum at 60 sec corresponds to completion of the first monolayer and exposure is continued to about 160 monolayers (10 000 sec). The specular signal prior to exposure was about 1.5×10^8 counts/sec.

Figure 2 shows two angular distributions for an incident energy of 10.4 meV and a surface temperature $T_s=40$ K obtained from the freshly grown Xe(111) surface along the Pt(111) high symmetry directions $[1\bar{1}0]$ and $[11\bar{2}]$. The diffraction spots do not exhibit any splitting which would indicate the presence of domains in the Xe film that are rotated relative to each other and to the substrate high symmetry directions. The absence of the two Novaco-McTague rotated[39] Xe adlayer domains observed earlier for monolayers[6,35] and multilayers[6] is presumably due to a somewhat higher step density on the present Pt(111) surface. Hence, the Pt(111) surface directions $[1\bar{1}0]$ and $[11\bar{2}]$ correspond to the Xe(111) $\bar{\Gamma}$-$\bar{M}$ and $\bar{\Gamma}$-$\bar{K}$ azimuths in the first surface Brillouin zone (SBZ), respectively, indicating that the Xe(111) surface is rotated by 30° with respect to the Pt(111) surface. Further, the angular distributions show that the surface of 160 monolayers of xenon on Pt(111) at $T_s=40$ K is hexagonal with a unit cell size of $a=4.37$ Å . This corresponds to the (111) face of fcc xenon, although the lattice constant is 0.04 Å larger than the value of $a=4.33$ Å previously reported for the surface at $T_s=25$ K.[4,5] This difference arises from thermal expansion of the adlayer due to the higher temperature used in the present experiments. As shown in Fig. 2, the first order diffraction peak intensities are a factor of 4–10 smaller than the specular peak, indicating a moderately corrugated He-Xe(111) surface potential.[40,41]

Figure 3 shows a series of TOF measurements in which

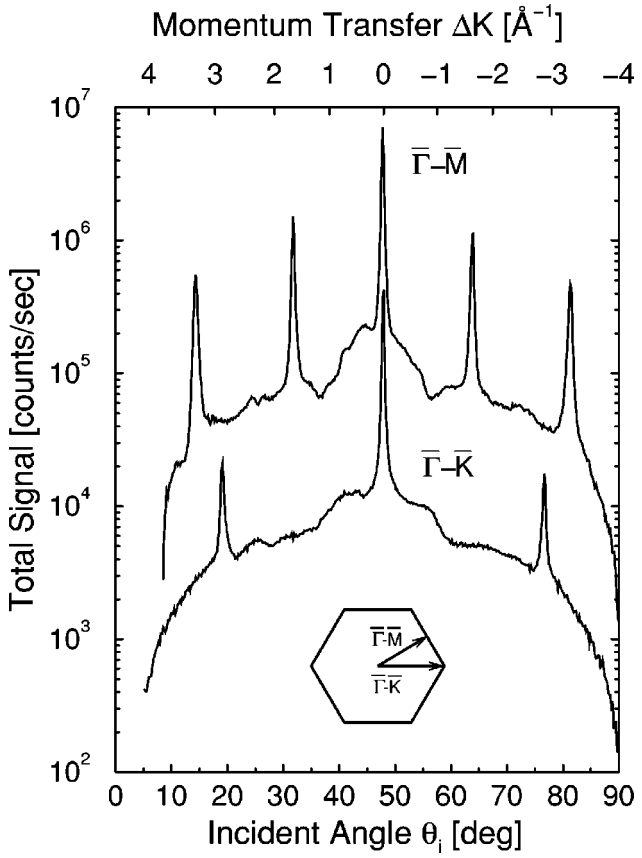

FIG. 2. Helium scattering angular distributions for the $\bar{\Gamma}$-$\bar{M}$ and $\bar{\Gamma}$-$\bar{K}$ azimuths of the Xe(111) surface at $T_s=40$ K and an incident energy of $E_i=10.4$ meV. The upper distribution ($\bar{\Gamma}$-$\bar{M}$) has been offset by a factor of 10 for clarity. The specular peak is located at $\theta_i=47.9°$. The intense diffraction peaks at $\Delta K=\pm 1.66$ Å^{-1}, $\Delta K=\pm 3.32$ Å^{-1} ($\bar{\Gamma}$-$\bar{M}$), and $\Delta K=\pm 2.88$ Å^{-1} ($\bar{\Gamma}$-$\bar{K}$) indicate a regular hexagonal unit cell with a surface lattice constant of $a=4.37$ Å. The uneven background under the diffraction peaks is attributed to variations in the inelastic intensity which is a significant contribution to the total signal.

the flight time has been converted to energy transfer ΔE, along the Xe(111) $\bar{\Gamma}$-$\bar{M}$ azimuth for a low beam energy of $E_i=5.5$ meV and a surface temperature of $T_s=50$ K. The most dominant peaks are the incoherent elastic peaks at zero energy transfer ($\Delta E=0$) which correspond to scattering from defects in the Xe(111) surface, such as adatoms, vacancies, and steps. In addition to the incoherent elastic peak other dispersive peaks on both energy gain and loss sides are clearly visible. From a comparison with the results reported previously for 25 monolayers,[3–8] the dispersive peaks can be assigned to the Xe(111) Rayleigh wave phonons (RW). As can be seen from the TOF spectra in Fig. 3, the Rayleigh phonon intensity does not decrease monotonically with angle from the specular peak at $\theta_i=47.9°$. This is most clearly seen for the energy loss peaks in Fig. 3(b) in which the Rayleigh wave and diffuse elastic peak intensities exhibit a different variation with the incident angle θ_i. Previously for the Cu(111) (Refs. 42,43) and Rh(111) (Ref. 44) systems the RW inelastic peak intensities were observed to decrease

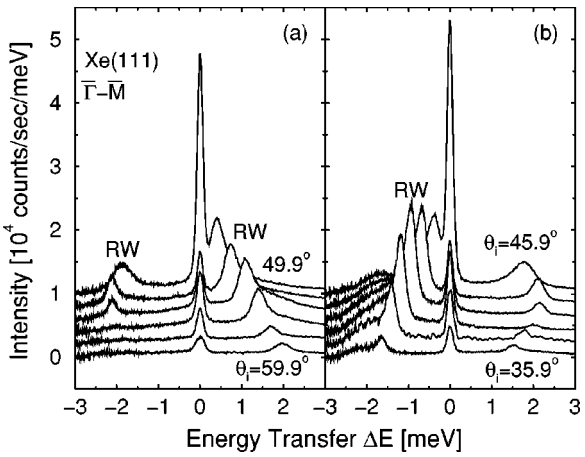

FIG. 3. Several time-of-flight spectra for incident angles greater than specular ($\theta_i=47.9°$) (a) and less than specular (b) for helium scattering from the Xe(111) surface along the $\bar{\Gamma}$-$\bar{M}$ azimuth. The spectra are separated by an angle of 2° and have been converted from flight time to energy transfer scale. The incident energy was $E_i=5.5$ meV and the surface temperature was $T_s=50$ K. In addition to the diffuse elastic peak at $\Delta E=0$, the dispersive Xe(111) surface Rayleigh phonon (RW) can be clearly seen for both energy loss and gain. The spectra are vertically offset from each other by 2000 counts/sec/meV for clarity.

monotonically with increasing angles for incident energies $E_i \gtrsim 15$ meV.

Time-of-flight measurements were also made along the Xe(111) $\bar{\Gamma}$-$\bar{K}$ direction for an incident energy of $E_i=5.7$ meV and a surface temperature $T_s=40$ K. Several spectra are shown in Fig. 4. As for the $\bar{\Gamma}$-$\bar{M}$ azimuth, the Rayleigh

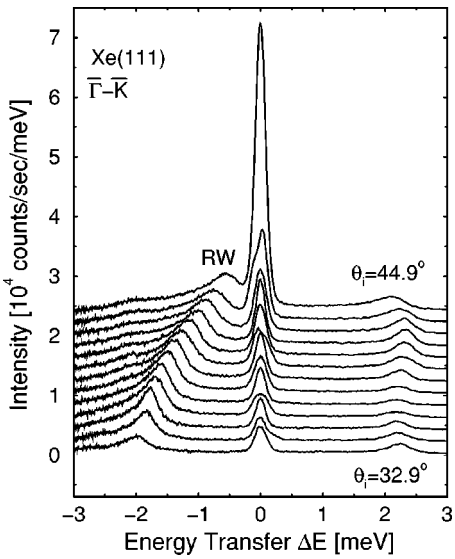

FIG. 4. Several time-of-flight spectra separated by $\Delta\theta_i=1°$ for helium scattering from the Xe(111) surface along the $\bar{\Gamma}$-$\bar{K}$ azimuth. The incident energy was $E_i=5.7$ meV and the surface temperature was $T_s=40$ K. In addition to the incoherent elastic peak at $\Delta E=0$, the dispersive Xe(111) surface Rayleigh phonon (RW) can be clearly seen for both energy loss and gain. The spectra are vertically offset from each other by 2000 counts/sec/meV for clarity.

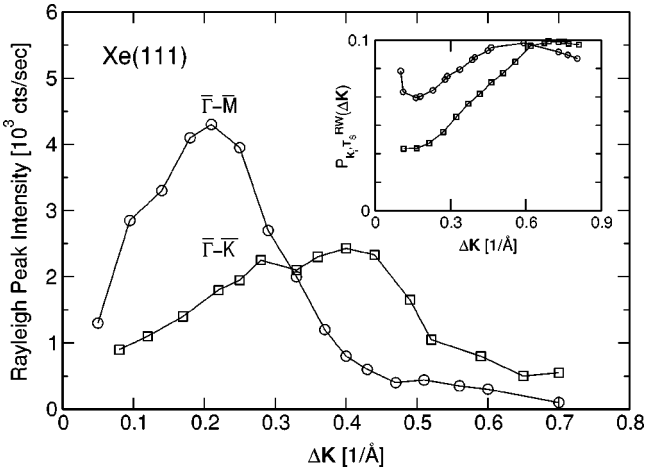

FIG. 5. Experimental Rayleigh phonon peak intensity (peak area) for positive momentum transfer ($\Delta K>0$) and energy loss ($\Delta E<0$) for the $\bar{\Gamma}$-$\bar{M}$ (circles) and $\bar{\Gamma}$-$\bar{K}$ (squares) azimuths. The incident energy was $E_i=5.5$ meV and the surface temperature was $T_s=40$ K. Inset: theoretical Rayleigh peak excitation probabilities $P^{\mathrm{RW}}_{\mathbf{k}_i,T_s}(\Delta\mathbf{K})$ (denoted by the same symbols for the same experimental conditions) calculated in the flat surface approximation, as discussed in Sec. VI.

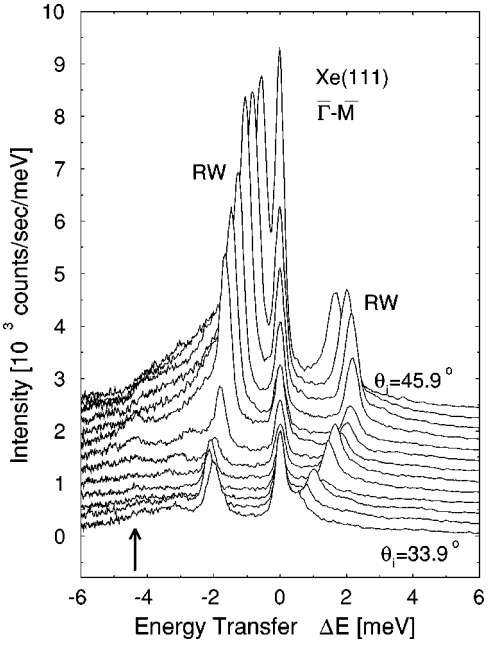

FIG. 6. Several time-of-flight spectra separated by $\Delta\theta_i=1°$ for helium scattering from the Xe(111) surface along the $\bar{\Gamma}$-$\bar{M}$ azimuth. The incident energy was $E_i=10.5$ meV and the surface temperature was $T_s=40$ K. In addition to the diffuse elastic peak at $\Delta E=0$, the dispersive Xe(111) surface Rayleigh phonon (RW) can be clearly seen for both energy loss and gain, as well as several less intense peaks up to $\Delta E=-4.3$ meV (indicated by an upward directed arrow) in some of the spectra. The spectra are vertically offset from each other for clarity.

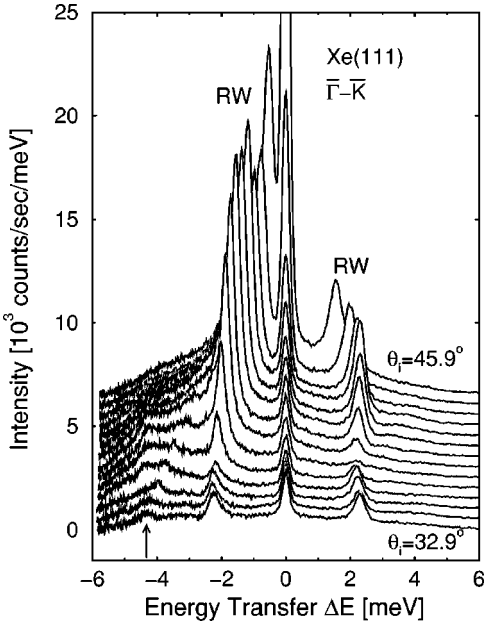

FIG. 7. Several time-of-flight spectra separated by $\Delta\theta_i=1°$ for helium scattering from the Xe(111) surface along the $\bar{\Gamma}$-$\bar{K}$ azimuth. The incident energy was $E_i=10.2$ meV and the surface temperature was $T_s=40$ K. In addition to the diffuse elastic peak at $\Delta E=0$, the dispersive Xe(111) surface Rayleigh phonon (RW) peaks at both the energy loss and gain sides, a nondispersive mode at about -4.3 meV (indicated by an upward directed arrow) is clearly discernible. The spectra are vertically offset from each other for clarity.

phonon peaks can be seen for both energy loss and gain. In addition, the Rayleigh phonon peak intensity was observed to increase for angles of incidence close to the specular peak and decrease for larger angles.

The Rayleigh phonon intensities (peak areas) for the $\bar{\Gamma}$-$\bar{M}$ and $\bar{\Gamma}$-$\bar{K}$ azimuths for positive momentum and negative energy transfers with an incident energy of $E_i=5.5$ meV are shown in Fig. 5. Along the $\bar{\Gamma}$-$\bar{M}$ direction the Rayleigh mode has a maximum at $\Delta K\simeq 0.2$ Å^{-1} whereas the maximum along the $\bar{\Gamma}$-$\bar{K}$ is somewhat broader and occurs at $\Delta K\simeq 0.4$ Å^{-1}.

As can be seen from the spectra in Figs. 3 and 4, only the low-frequency Rayleigh phonon modes are excited at the low incident energy of 5.5 meV. In order to excite the SH and L surface phonons which lie at higher frequencies, the incident beam energy was increased to $E_i=10.5$ meV similar to the energies used in the earlier monolayer experiments.[35] Figure 6 shows several TOF spectra at a surface temperature of $T_s=40$ K along the $\bar{\Gamma}$-$\bar{M}$ azimuth for incident angles between $\theta_i=33.9°$ and $\theta_i=45.9°$. As for the measurements at $E_i=5.5$ meV, the relative intensity of the Rayleigh mode (RW) peaks varies significantly with incident angle, particularly on the energy gain side. However, in addition to the Rayleigh mode, additional inelastic peaks can be observed in several of the spectra. In particular for $\theta_i=39.9°$, additional peaks are seen at $\Delta E=-2.7$ meV and $\Delta E=-4.3$ meV. Figure 7 shows a similar set of TOF spectra for the $\bar{\Gamma}$-$\bar{K}$

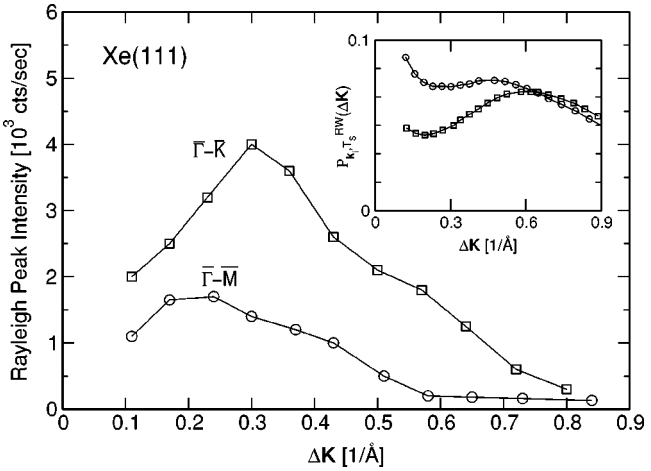

FIG. 8. Experimental Rayleigh phonon peak intensity (peak area) for positive momentum transfer ($\Delta K>0$) and energy loss ($\Delta E<0$) for the $\bar{\Gamma}$-$\bar{M}$ (circles) and $\bar{\Gamma}$-$\bar{K}$ (squares) azimuths. The incident energy was $E_i=10.5$ meV and the surface temperature was $T_s=40$ K. Inset: theoretical Rayleigh peak excitation probabilities $P^{\mathrm{RW}}_{\mathbf{k}_i,T_s}(\Delta\mathbf{K})$ (denoted by the same symbols for the same experimental conditions) calculated in the flat surface approximation, as discussed in Sec. VI.

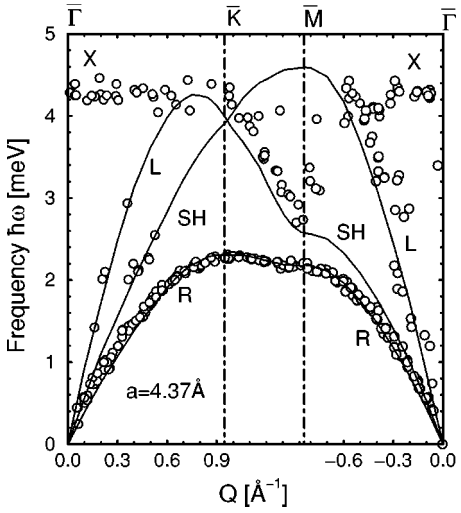

FIG. 9. The Xe(111) surface phonon dispersion curves determined from HAS time-of-flight measurements for incident energies of $E_i=5.5$ meV and 10.5 meV (open circles) shown on a reduced zone scheme. The solid curves show the results of calculations for the Rayleigh phonon (R), Longitudinal acoustic (L), and shear horizontal (SH) modes. A further dispersionless mode (X) at $\hbar\omega=4.3$ meV is also observed.

azimuth and an incident energy of 10.2 meV. An interesting feature of the displayed TOF spectra is the peak at about $\Delta E=-4.3$ meV which is particularly visible at smaller incident angles. At intermediate angles the intensity of the Rayleigh wave exceeds the intensity of the incoherent elastic peak, whereas all the other inelastic features are significantly less intense.

The Rayleigh phonon peak areas for the $\bar{\Gamma}$-$\bar{M}$ and $\bar{\Gamma}$-$\bar{K}$ azimuths for a higher incident energy of $E_i=10.5$ meV are shown in Fig. 8. At the higher energy the $\bar{\Gamma}$-$\bar{K}$ azimuth shows a greater intensity than the $\bar{\Gamma}$-$\bar{M}$ direction and the intensity maxima are at about the same momentum transfers as at the lower energy. The Rayleigh mode along the $\bar{\Gamma}$-$\bar{M}$ direction has its maximum at about the same value of $\Delta K\simeq 0.2$ Å^{-1} whereas the maximum along the $\bar{\Gamma}$-$\bar{K}$ direction is shifted slightly to a smaller value of $\Delta K\simeq 0.3$ Å^{-1}.

The energy losses and gains from the TOF spectra along the $\bar{\Gamma}$-$\bar{M}$ and $\bar{\Gamma}$-$\bar{K}$ azimuths for the incident energies $E_i=5.5$ and 10.5 meV fall together on the same curves as shown in Fig. 9 on a reduced zone scheme. The majority of the inelastic peaks are from the intense Rayleigh wave while the less intense dispersive modes, which are observed along both directions, lie at higher frequencies. In addition, a broad dispersionless feature at about $\hbar\omega=4.3$ meV (denoted by X) is also evident along both azimuths, particularly close to the $\bar{\Gamma}$ points.

IV. THE BORN–VON KÁRMÁN CALCULATION OF THE SURFACE PHONON DISPERSION CURVES

The phonon dispersion curves and polarization vectors for the present system were calculated using the Born–von Kármán force constant scheme in which the Xe crystal is modeled by a 80 atom thick fcc slab bounded by (111) surfaces on each side.[45] Three-body Xe interactions were neglected and the HFD-B2 pair potential of Aziz *et al.*[36] was used, since this potential provided a good description of the phonons in Xe monolayers on a Pt(111) surface.[35,46] In the present calculations the nearest neighbor Xe-Xe equilibrium distance is fixed at $a=4.37$ Å, the value determined from He atom diffraction measurements (see Fig. 2) at the same substrate temperature as for the inelastic scattering experiments. Further, in the present dynamical matrix model all the effects due to perpendicular relaxation of the Xe(111) surface are neglected because relaxation of the rare gas fcc(111) surfaces has been found to be small in this model.[45] The radial β and tangential α force constants corresponding to the first and second nearest neighbor atoms are listed in Table I.

To introduce the normal modes of the system into the model we define a three-dimensional (3D) unit cell which extends from one surface of the slab to the other.[45] The complete slab is generated by applying the two-dimensional (2D)

TABLE I. The values of the radial, β, and tangential, α, force constants for the first (1) and second (2) nearest neighbors in the fcc xenon crystal used in the present analysis. The values were obtained from the HFD-B2 potential (Ref. 36) using the experimental interatomic distance of $a=4.37$ Å obtained for substrate temperature $T_s=40$ K.

Force constant	Value (N/m)
β_1^{Xe-Xe}	1.636
β_2^{Xe-Xe}	−0.088
α_1^{Xe-Xe}	0.002
α_2^{Xe-Xe}	0.012

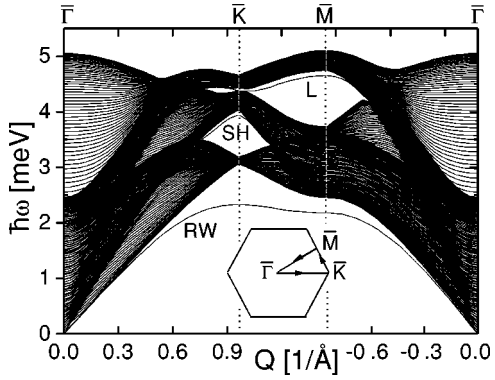

FIG. 10. Calculated phonon dispersion curves as a function of the two-dimensional wave vector Q along the boundary $\bar{\Gamma}\rightarrow\bar{K}\rightarrow\bar{M}\rightarrow\bar{\Gamma}$ of the irreducible part of the first surface Brillouin zone (SBZ) of an 80 layer fcc Xe slab with (111) surfaces. The zone boundary vectors are $\bar{\Gamma}$-$\bar{K}$=0.958 Å^{-1}, $\bar{K}$-$\bar{M}$=0.83 Å^{-1}, and $\bar{\Gamma}$-$\bar{M}$=0.479 Å^{-1}. Three surface localized modes detached from the bulk continuum are clearly discernible; the dominantly perpendicularly or *Z*-polarized Rayleigh wave below the bulk continuum, the dominantly shear-horizontally polarized or SH mode in the gap around the $\bar{K}$ point (this mode becomes degenerate with the bulk continuum in the remainder of the SBZ), and the dominantly longitudinally polarized or L mode in the gap extending from $\bar{K}$ to $\bar{M}$ points of the SBZ, and turning into a longitudinal resonance in the remainder of the SBZ.

translation group and the entire slab has a periodic 2D structure in the directions parallel to the surface. The equilibrium position of an atom in the slab is described by $\mathbf{r}_{l,\kappa}=(\mathbf{R}_l+\mathbf{R}_\kappa,z_\kappa)$, where the 2D vector $\mathbf{R}_l$, which is parallel to the (x,y) plane of the surface, is associated with the lth unit cell. $(\mathbf{R}_\kappa,z_\kappa)$ is the basis vector in the unit cell which gives the position of the κth atom in the layer fixed by the perpendicular coordinate z_κ, where $\kappa=1$ denotes the topmost layer. $\mathbf{u}_{l,\kappa}=(\mathbf{u}_{l,\kappa\parallel},u_{l,\kappa\perp})$ denotes the displacement of the (l,κ)th Xe atom from equilibrium position at $\mathbf{r}_{l,\kappa}$ and the periodicity of the slab in the directions parallel to the surface is exploited in order to represent $\mathbf{u}_{l,\kappa}$ as a Fourier series in terms of normal modes in the slab. The normal mode vibrational frequencies $\omega_{\mathbf{Q},j}$ and orthonormalized polarization vectors $\mathbf{e}_\kappa(\mathbf{Q},j)$ associated with a κth layer, which are functions of 2D phonon wave vector $\mathbf{Q}$ and a branch index j, are obtained as solutions of the standard dynamical matrix.[45]

The phonon dispersion curves calculated for a slab consisting of 80 Xe layers using the force constants listed in Table I are presented in Fig. 10. The dispersion curve of the surface localized phonon which develops from the S mode in monolayer solids[45] is detached from the lower edge of the bulk continuum over the entire irreducible part of the hexagonal first surface Brillouin zone (SBZ). This phonon is dominantly vertically or *Z* polarized and therefore can be identified with the Rayleigh wave. In addition, some surface projected modes are also discernible in the gaps of the bulk continuum whereas others appear as resonances in the continuum. These in-plane surface modes can be assigned either the longitudinal (L) or the shear horizontal (SH) character according to the relative directions of their polarization and

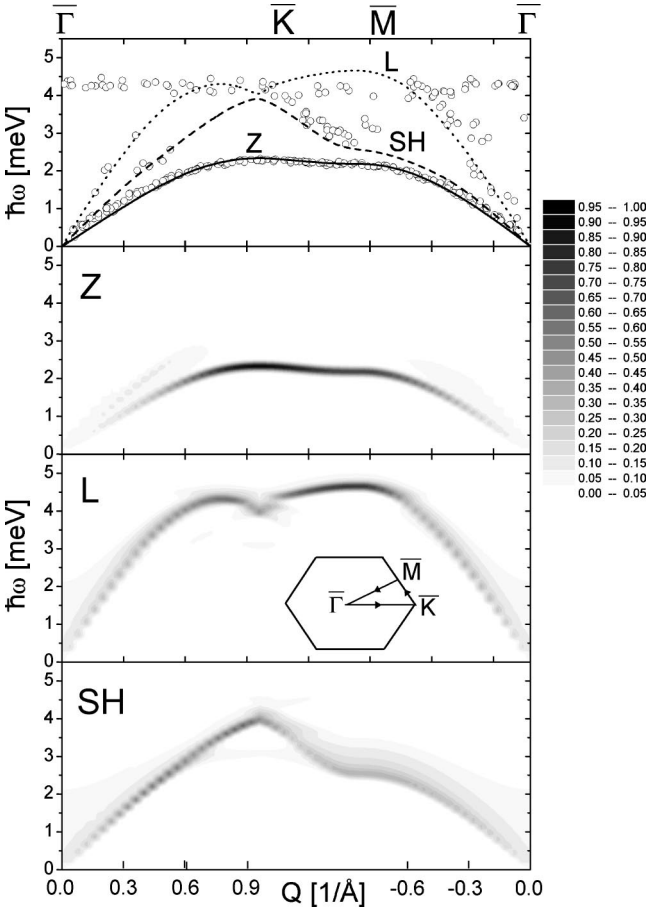

FIG. 11. Top panel: The experimental Xe(111) surface dispersion curves (open circles) from Fig. 9 shown on a reduced zone scheme are compared with the maxima of the surface projected phonon densities of states calculated from Eq. (2) for vertical (Z), in-plane longitudinal (L), and in-plane shear horizontal (SH) polarization which are denoted by the solid, long dashed, and short dashed lines, respectively. The lower panels display separately the Z-, L-, and or SH-polarized density of phonon states projected onto the topmost layer of Xe atoms in the slab, as calculated by the dynamical matrix method described in Sec. IV. Comparison with the upper panel reveals the polarization properties of the three experimentally detected surface projected modes in the first SBZ and enables their identification with the Rayleigh wave (RW), longitudinal (L), and shear horizontal (SH) modes. The scale of the DOS maxima [$\leqslant 1$, see Eq. (2) and thereafter] is given on the left ordinate.

wave vectors. This is illustrated by calculating and plotting the Z-, L-, and SH-projected phonon densities of states (DOS) defined by

$$\mathcal{D}_i(\omega,\mathbf{Q})=\sum_j |(\mathbf{e}_{\kappa=1}(\mathbf{Q},j))_i|^2\,\delta(\omega-\omega_{\mathbf{Q},j}), \qquad (2)$$

where i denotes the Z, L, or SH polarization and j ranges over all mode branches in the slab.

Figure 11 compares the measured dispersion points with the calculated surface-projected phonon DOS defined in Eq. (2) for the three surface modes. In plotting the calculated results each δ function on the RHS of Eq. (2) was replaced

by a Gaussian of width 0.19 meV to consistently model the experimental resolution. In this case the maxima of the thus integrated phonon DOS cannot exceed unity because of the orthonormality of the mode polarization vectors. These DOS plots clearly demonstrate that the most intense phonon branch is the dominantly Z-polarized Rayleigh mode. However, it should also be observed that along the $\overline{\Gamma}$-$\overline{K}$ direction the surface modes with SH polarization also exhibit a weak Z-polarization component which may make their detection possible for this scattering direction. The comparison also indicates that the mode, which is observed in the bulk continuum gap between the $\overline{K}$ and $\overline{M}$ points (see Fig. 10), is dominantly L polarized.

V. CALCULATION OF THE INELASTIC INTENSITIES

The calculation of the intensities for scattering of He atoms from phonons of the Xe(111) surface will be carried out within the appropriately modified theoretical formalism developed in Refs. 32 and 47. The application of this formalism to the present problem requires a careful examination and modeling of the He-surface interaction potential $U(\mathbf{r},\{\mathbf{u}_{l,\kappa}\})$ which depends on the position vector $\mathbf{r}$ of the He atom, and on the equilibrium positions $\mathbf{r}_{l,\kappa}$ and displacements $\mathbf{u}_{l,\kappa}$ of the atoms in the crystal. In this section we present a generalization of the model outlined in Ref. 32 so as to account for projectile interactions with all the atoms of the Xe van der Waals crystal. Thus, the total He-Xe crystal potential is assumed to be a pairwise addition of two-body gas phase He-Xe potentials $v(\mathbf{r}-\mathbf{r}_{l,\kappa}-\mathbf{u}_{l,\kappa})$, whose dependence on the spatial coordinates can be modeled by using expressions from either Ref. 48 or Ref. 49. For the present purposes both potentials yield practically indistinguishable results. The resulting total He-Xe(111) potential can be written as

$$U(\mathbf{r},\{\mathbf{u}_{l,\kappa}\})=U_{\mathrm{stat}}(\mathbf{r})+V(\mathbf{r},\{\mathbf{u}_{l,\kappa}\}), \tag{3}$$

where $U_{\mathrm{stat}}(\mathbf{r})$ is the static He atom-Xe crystal interaction obtained by setting all displacements $\mathbf{u}_{l,\kappa}$ equal to zero, viz.

$$U_{\mathrm{stat}}(\mathbf{r})=\sum_{l,\kappa} v(\mathbf{r}-\mathbf{r}_{l,\kappa}). \tag{4}$$

The dynamic interaction contained in the term $V(\mathbf{r},\{\mathbf{u}_{l,\kappa}\})$ is obtained from the expansion of the total potential in a Taylor series of which only the terms linear in the displacements are retained:

$$V(\mathbf{r},\{\mathbf{u}_{l,\kappa}\})=\sum_{l,\kappa}\left[-\nabla_{\mathbf{r}}v(\mathbf{r}-\mathbf{r}_{l,\kappa})\right]\cdot\mathbf{u}_{l,\kappa}=\sum_{l,\kappa}\mathbf{F}_{l,\kappa}(r)\cdot\mathbf{u}_{l,\kappa}. \tag{5}$$

The $\mathbf{F}_{l,\kappa}(\mathbf{r})$ are the forces exerted by the crystal atom at $\mathbf{r}_{l,\kappa}$ on the projectile atom at $\mathbf{r}$.

As in our earlier studies of inelastic scattering from monolayer Xe surfaces,[32] the effect of the corrugation of the static potential, Eq. (4), on *inelastic* He atom transitions is neglected and only the surface average of the potential of Eq. (4) is accounted for. To obtain the surface averaged static potential for the present system, the He atom interaction with the topmost layer $\kappa=1$ of Xe atoms was first calculated using the potentials from Refs. 48 and 49 to yield

$$U_{\kappa=1}(z)=\frac{1}{A_c}\int_{\mathrm{sur}} v(\mathbf{r})d^2\mathbf{R}, \tag{6}$$

where A_c is the area of the 2D surface unit cell. The contributions from the κth layers in the crystal are approximated by assuming the following generalized Morse potential:

$$U_{\kappa}^{\mathrm{fit}}(z)=D[(1-e^{-2b/d})e^{-2[z+(\kappa-1)b-z_0]/d} -2(1-e^{-b/d})e^{-[z+(\kappa-1)b-z_0]/d}], \tag{7}$$

where b is the normal distance between two adjacent equivalent Xe(111) planes ($b=\sqrt{2/3}a=3.568$ Å). The parameters D and d were determined by a best fit to the values of the topmost layer potential $U_1(z)$ in the interval around the turning point, with the requirement that the fitted potential correctly reproduces the value at the potential minimum obtained from the numerical integration of Eq. (6). The potential in Eq. (7) is then summed over all subsequent underlying layers to finally yield the laterally averaged static He-Xe(111) potential in the Morse form

$$U_{\mathrm{stat}}(z)=\sum_{\kappa=1}^{\infty} U_{\kappa}^{\mathrm{fit}}(z)=D[e^{-2(z-z_0)/d}-2e^{-(z-z_0)/d}]. \tag{8}$$

The parameters of the potential $U_{\mathrm{stat}}(z)$ obtained using this procedure are listed in Table II.

TABLE II. Parameters for the potential $U_{\mathrm{stat}}(z)$ in Eqs. (7) and (8).

D (meV)	d (Å)	z_0 (Å)	b (Å)
5.625	0.641	3.514	3.572

The computation of the matrix elements needed in the calculation of inelastic scattering intensities is now greatly simplified since the Schrödinger equation with the potential of Eq. (8) can be solved analytically to yield the distorted waves

$$\langle\mathbf{r}|\mathbf{k}\rangle=\langle\mathbf{R},z|\mathbf{K},k_z\rangle=\frac{1}{\sqrt{L_zL_s^2}}\exp(i\mathbf{KR})\chi_{k_z}(z), \tag{9}$$

which describe the elastic projectile motion in the static surface potential $U_{\mathrm{stat}}(z)$ (Refs. 50–54) and satisfy the normalization $\langle\mathbf{k}|\mathbf{k}'\rangle=\delta_{\mathbf{k},\mathbf{k}'}$. Here L_s and L_z are the quantization lengths in the directions parallel and perpendicular to the surface, respectively, $\mathbf{K}$ is the wave vector describing unperturbed projectile motion parallel to the surface, and k_z plays the role of the quantum number describing the motion in the direction perpendicular to the surface so that the perpendicular energy $E_z\rightarrow\hbar^2k_z^2/2M$ for $z\rightarrow\infty$.

Equations (3)–(9) provide the necessary ingredients for defining the inelastic scattering spectrum $N(\Delta E,\Delta\mathbf{K})$ which gives the probability density that amounts of energy ΔE

$=E_f-E_i$ and parallel momenta $\Delta\mathbf{K}=\mathbf{K}_f-K_i$ are transferred from the He atom to the substrate phonons.[32,47,55] For the current experimental conditions the uncorrelated phonon exchange processes dominate over the correlated ones[47] and the latter are neglected altogether. In this regime the angular resolved scattering spectrum, which depends parametrically on the surface temperature T_s and initial projectile momentum $\hbar\mathbf{k}_i$, can then be accurately calculated using the exponentiated Born approximation (EBA) scattering formalism.[56–58] This yields the EBA scattering spectrum[47]

$$N^{\mathrm{EBA}}_{\mathbf{k}_i,T_s}(\Delta E,\Delta\mathbf{K})=\int_{-\infty}^{\infty}\frac{d\tau\, d^2\boldsymbol{\mathcal{R}}}{(2\pi\hbar)^3}e^{(i/\hbar)[(\Delta E)\tau-\hbar(\Delta\mathbf{K})\boldsymbol{\mathcal{R}}]}\times\exp[2W^{\mathrm{EBA}}_{\mathbf{k}_i,T_s}(\boldsymbol{\mathcal{R}},\tau)-2W^{\mathrm{EBA}}_{\mathbf{k}_i,T_s}(0,0)], \tag{10}$$

where τ and $\boldsymbol{\mathcal{R}}=(X,Y)$ are the variables of the so-called EBA scattering or driving function $2W^{\mathrm{EBA}}_{\mathbf{k}_i,T_s}(\boldsymbol{\mathcal{R}},\tau)$, explicitly given below [see Eq. (12)], which contains all the information on uncorrelated phonon exchange processes in the atom-surface scattering event. After carrying out the $(\tau,\boldsymbol{\mathcal{R}})$-Fourier transform on the right-hand side (RHS) of Eq. (10) the values of $\Delta\mathbf{K}$ and ΔE are confined to the scan curve. This yields the theoretical intensities as the function of ΔE which can be compared with the experimental HAS TOF intensities.[59]

The value $2W^{\mathrm{EBA}}_{\mathbf{k}_i,T_s}(\boldsymbol{\mathcal{R}}=0,\tau=0)=2W^{\mathrm{EBA}}_{\mathbf{k}_i,T_s}$ gives the EBA expression for the Debye-Waller exponent (DWE) pertaining to the present inelastic scattering model. It has also been shown[57] that this DWE represents the mean number of phonons excited in all inelastic scattering events with projectile initial momentum $\hbar\mathbf{k}_i$ and substrate temperature T_s. The corresponding Debye-Waller factor (DWF) given by $\exp[-2W^{\mathrm{EBA}}_{\mathbf{k}_i,T_s}]$ represents, according to Eq. (10), a common attenuating factor for all the spectral features in $N^{\mathrm{EBA}}_{\mathbf{k}_i,T_s}(\Delta E,\Delta\mathbf{K})$ for particular initial conditions $\mathbf{k}_i$ and T_s. The spectrum (10) also includes the elastically scattered specular beam intensity which is given by[60,61]

$$[N^{\mathrm{EBA}}_{\mathbf{k}_i,T_s}(\Delta E,\Delta\mathbf{K})]_{\mathrm{specular}}=e^{-2W^{\mathrm{EBA}}_{\mathbf{k}_i,T_s}}\delta(\Delta E)\,\delta(\Delta\mathbf{K}). \tag{11}$$

In the present approach, in which only the linear projectile-phonon coupling, Eq. (5), is retained in Eq. (3), the EBA scattering function in Eq. (10) takes the form[47]

$$2W^{\mathrm{EBA}}_{\mathbf{k}_i,T_s}(\boldsymbol{\mathcal{R}},\tau)=\sum_{\mathbf{Q},\mathbf{G},j,k'_z}[|\mathcal{V}^{\mathbf{K}_i,\mathbf{Q}+\mathbf{G},j}_{k'_z,k_{zi}}(+)|^2\times[\overline{n}(\hbar\omega_{\mathbf{Q},j})+1]e^{-i[\omega_{\mathbf{Q},j}\tau-(\mathbf{Q}+\mathbf{G})\boldsymbol{\mathcal{R}}]}+|\mathcal{V}^{\mathbf{K}_i,\mathbf{Q}+\mathbf{G},j}_{k'_z,k_{zi}}(-)|^2\overline{n}(\hbar\omega_{\mathbf{Q},j})\times e^{i[\omega_{\mathbf{Q},j}\tau-(\mathbf{Q}+\mathbf{G})\boldsymbol{\mathcal{R}}]}]. \tag{12}$$

Here $\overline{n}(\omega_{\mathbf{Q},j})$ is the Bose-Einstein distribution of phonons of energy $\hbar\omega_{\mathbf{Q},j}$ at the substrate temperature T_s, and the one-phonon emission $(+)$ and absorption $(-)$ scattering amplitudes $\mathcal{V}^{\mathbf{K}_i,\mathbf{Q}+\mathbf{G},j}_{k'_z,k_{zi}}(\pm)$ are calculated from the projectile-phonon interaction matrix elements $V^{\mathbf{K}_i,\mathbf{Q}+\mathbf{G},j}_{k'_z,k_{zi}}$ by confining them to the energy shell and normalizing the resulting values to the projectile current normal to the surface.[32,47] The matrix elements $V^{\mathbf{K}_i,\mathbf{Q}+\mathbf{G},j}_{k'_z,k_{zi}}$ of the inelastic interaction potential (5) are expressed in terms of the two-dimensional Fourier transform $v_{\mathbf{Q}+\mathbf{G}}(z-z_\kappa)$ of the atomic pair potentials

$$V^{\mathbf{K}_i,\mathbf{Q}+\mathbf{G},j}_{k'_z,k_{zi}}=\sum_{\kappa=1}^{2}\left(\frac{\hbar}{2NM_{Xe}\omega_{\mathbf{Q},j}}\right)^{1/2}\int dz\,\chi^*_f(z)\mathbf{e}_\kappa(\mathbf{Q},j)\times\left[-i(\mathbf{Q}+\mathbf{G}),\hat{\mathbf{z}}\frac{\partial}{\partial z}\right]v_{\mathbf{Q}+\mathbf{G}}(z-z_\kappa)\chi_i(z), \tag{13}$$

where M_{Xe} is the mass of a Xe atom and only the first and second layer corresponding to $\kappa=1,2$ were included in Eq. (13) since they give the dominant contribution. The expression in the square brackets in the integrand on the RHS of Eq. (13) derives from the gradient operator in Eq. (5) and $\hat{\mathbf{z}}$ denotes the unit vector perpendicular to the surface. Here, following the procedure of Bortolani and co-workers[62,63] and consistent with expression (7), the $\mathbf{Q}$ dependence of $v_{\mathbf{Q}}(z)$ leading to expression (8) is, to a good approximation, represented by a Gaussian cutoff arising from the simultaneous interaction of the projectile with several substrate atoms. This yields

$$v_{\mathbf{Q}}(z-z_\kappa)=A_cD[(1-e^{-2b/d})e^{-2[z+(\kappa-1)b-z_0]/d}e^{-Q^2/2Q_c^2}-2(1-e^{-b/d})e^{-[z+(\kappa-1)b-z_0]/d}e^{-Q^2/Q_c^2}], \tag{14}$$

with $Q_c=\sqrt{2/z_td}$ and where z_t is the energy dependent classical turning point for the projectile motion in front of the surface.

The scalar product on the RHS of Eq. (13), viz.

$$\mathbf{e}_\kappa(\mathbf{Q},j)\left[-i(\mathbf{Q}+\mathbf{G}),\mathbf{z}_0\frac{\partial}{\partial z}\right] \tag{15}$$

indicates that the strongest dynamical coupling near the $\overline{\Gamma}$ point will occur with the vertical or the Z component of the polarization vectors of the three surface modes, and that the coupling to the longitudinally polarized modes will be greatest away from the $\overline{\Gamma}$ point (i.e., for larger $\mathbf{Q}+\mathbf{G}$). The coupling of He atoms to SH modes for the case of in-sagittal-plane scattering along the high symmetry direction $\overline{\Gamma}$-$\overline{M}$ in the first SBZ is identically equal to zero because in that scattering geometry the scalar product Eq. (15) vanishes. This selection rule is independent of the surface temperature and hence applies equally well to one-phonon emission and absorption in HAS from defect-free planar surfaces. However,

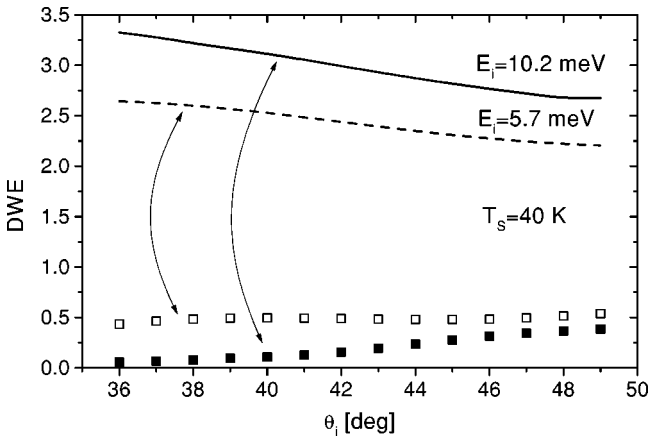

FIG. 12. The magnitude of the total phonon-induced Debye-Waller exponent (DWE), $2W^{\mathrm{EBA}}_{\mathbf{k}_i,T_s}$, as a function of He atom incident angle calculated for two experimental incident energies $E_i = 10.2$ meV (solid line) and $E_i = 5.7$ meV (dashed line), for fixed substrate temperature $T_s = 40$ K. The magnitudes of the contributions to the Debye-Waller exponents from He atom transitions into the bound states of the atom-surface potential $U_{\mathrm{stat}}(z)$ are denoted by filled and empty squares for the quoted two incident energies, respectively.

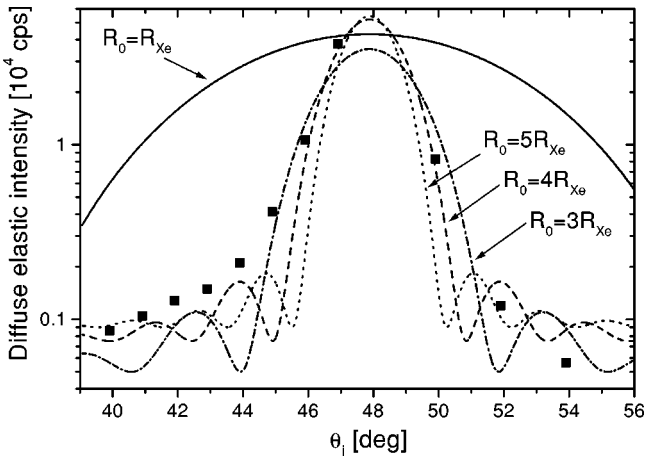

FIG. 13. The experimental diffuse elastic peak intensities $I^0_{\mathrm{diff}}(\theta_i)$, obtained by numerical integration of the elastic peak areas in the experimental TOF spectra for $E_i = 10.5$ meV in the $\overline{\Gamma}$-$\overline{K}$ direction are plotted as a function of the incident scattering angle. The full, dot-dashed, long dashed, and short dashed curves denote the fits through these points using Eq. (16) with $R_0 = 1$, 3, 4, and 5 R_{Xe}, respectively, where $2R_{\mathrm{Xe}}$ is the distance of the Xe-Xe pair potential well minimum.

the presence of surface defects relaxes the phonon momentum selection rule[64] and defect concentration may be temperature dependent.

Quite generally, the scattering spectrum calculated from Eq. (10) encompasses three distinct features arising from the $(\tau,\boldsymbol{\mathcal{R}})$-Fourier transform of the various terms in the power series expansion of $\exp[2W^{\mathrm{EBA}}_{\mathbf{k}_i,T_s}(\boldsymbol{\mathcal{R}},\tau)]$. The zeroth order term (i.e., unity) gives rise to the elastic peak described by Eq. (11), the first order or the distorted-wave Born approximation (DWBA) term gives rise to the single phonon features in the spectrum, and the remaining terms all contribute to the multiphonon background. It should also be noted that all three types of spectral features are multiplied by one and the same phonon-induced Debye-Waller factor $\exp[-2W^{\mathrm{EBA}}_{\mathbf{k}_i,T_s}]$ that depends on the incident projectile energy E_i, angle θ_i, and the substrate temperature T_s, but not on ΔE or $\Delta\mathbf{K}$. As the true multiphonon regime in which $2W^{\mathrm{EBA}}_{\mathbf{k}_i,T_s} \gg 1$ is reached, the weight of the no-loss line and one-phonon features is strongly suppressed by the Debye-Waller factor, while the multiphonon background, which tends to a Gaussian limit,[59] takes over the spectral weight.

VI. THEORETICAL INTERPRETATION AND DISCUSSION OF EXPERIMENTAL RESULTS

Before discussing the inelastic TOF spectra it is useful to first delineate the scattering regime in which the measurements were carried out and the effect of surface defects on the discussed inelastic scattering data. Since the phonon excitation energies in the heavy Xe system are relatively small, multiphonon excitations can take place even at low He beam incident energies. The scattering regime depends on the magnitude of the exponent of the phonon-induced Debye-Waller exponent $2W^{\mathrm{EBA}}_{\mathbf{k}_i,T_s}$ appearing in Eq. (10) and measuring the mean number of phonons exchanged with the heat bath in the course of the collision.[57] The Debye-Waller exponents calculated for the present scattering conditions are shown in Fig. 12 [compare with Fig. 12 in Ref. 32 for Xe monolayer on Cu(001)]. The points denoted by full and open squares indicate the contributions from inelastic, i.e., phonon assisted He atom transitions into the bound states of the projectile-surface potential. The calculated Debye-Waller exponents are greater than two in the whole range of the experimental incident angles, which means that even the measurements at $E_i = 5.5$ meV were carried out in the regime between single and multiphonon scattering. This explains the presence of the relatively large background intensities in the TOF spectra reported in Sec. III.

To establish the presence of defects such as adatoms, vacancies, small islands, or clusters on the surface, whose build up would be also consistent with reduction of the He specular signal for higher exposure times in Fig. 1, the diffuse elastic peak areas in the experimental TOF spectra were integrated numerically and plotted as a function of the incident angles θ_i between the zeroth and first order diffraction peaks. These values, denoted as $I^0_{\mathrm{diff}}(\theta_i)$ and shown as full squares in Fig. 13, were fitted to the following expression:

$$I^{\mathrm{fit}}_{\mathrm{diff}}(\theta_i) = AF(k_i, R_0, \theta_i, \theta_f) + B. \tag{16}$$

Here $F(k_i, R_0, \theta_i, \theta_f)$ is the Fraunhofer intensity for diffuse elastic scattering from a hemispherical defect with an effective radius R_0 on a planar surface as discussed in detail in Sec. IV of Ref. 65. The constants A and B, which depend on the effective defect density, were varied to obtain the fits of the ''experimental'' diffuse elastic scattering intensities with Eq. (16) for the $\overline{\Gamma}$-$\overline{K}$ direction with $E_i = 10.5$ meV and θ_i

$+\theta_f=\theta_{SD}$. The fits of the ''experimental'' intensity points in Fig. 13 indicate that the diffuse elastic intensities are consistent with the presence of defects with an effective radius in the range $3R_{Xe} \leqslant R_0 \leqslant 5R_{Xe}$ where $2R_{Xe}=4.36$ Å is the distance of the minimum of the Xe-Xe pair potential.[36]

A relevant issue arising in connection with the presence of clusters on the surface is the existence of vibrations localized at such defects. Although it is not possible to carry out a dynamical matrix analysis of the modes associated with the randomly distributed clusters, our additional dynamical matrix analyses have shown that the Xe atoms underneath single adatoms forming a (3×3) superstructure exhibit dominantly L-polarized quasilocalized modes whose frequencies in a back-folded first SBZ (or equivalently the first SBZ of the 3×3 superstructure) are nearly dispersionless at around 4 meV. Thus, it may be envisaged that modes of similar character may also exist along the circumference of adsorbed Xe islands or clusters and thus be observable in HAS.

In turning to the theoretical analyses of the TOF spectra we note that since only the spectra at $E_i=10.5$ meV exhibit, besides the Rayleigh waves, additional inelastic features their interpretation is of special interest. To this end we have first carried out the DWBA calculations of the one-phonon scattering intensities based on the model outlined in Sec. V in order to be able to make assignments for all well resolved peaks in the measured spectra, excluding only the peaks at $\Delta E=0$ which are due to incoherent scattering from surface defects not accounted for by the present EBA formalism. These DWBA calculations enable clear assignments of the RW, L, and SH modes in the measured spectra but are unable to explain the intensity of the dispersionless peak *X* clearly discernible at ~ -4.3 meV in some of the spectra for ΔK values close to the center of the first SBZ. Several complementary explanations of such incomplete description in the present DWBA calculations are possible. Thus, the appearance of the peak *X* can be associated with (i) spurions which have already been detected in the various earlier analyses of the HAS TOF spectra,[66–69] (ii) excitation of defect modes (localized phonons) since the presence of defects on the surface has been confirmed by the above analyses of the diffuse elastic peak intensities from the TOF spectra, (iii) multiphonon scattering processes whose intensities can be calculated only by going beyond the first order DWBA treatment of the scattering spectrum. Each of these explanations is plausible and we shall discuss them in order.

First, careful examinations of the scattering conditions and the scan curves corresponding to the TOF spectra shown in Figs. 6 and 7 enables to rule out spurions connected with the one-phonon processes[66–69] as a possible origin of the *X* peak. Second, single adatom defect modes, which are expected to have vibrational frequencies of less than 3 meV for the most favorable threefold hollow sites, can be also ruled out.[70] Hence, only the modes associated with clusters or islands, as was discussed at the beginning of this section, are possible candidates for the explanation of the origin of the *X* peak in some of the spectra. The examination of the third possibility, i.e., the multiphonon origin of the *X* peak, can be carried out on a rigorous quantitative level within the theoretical formalism outlined in Sec. V.

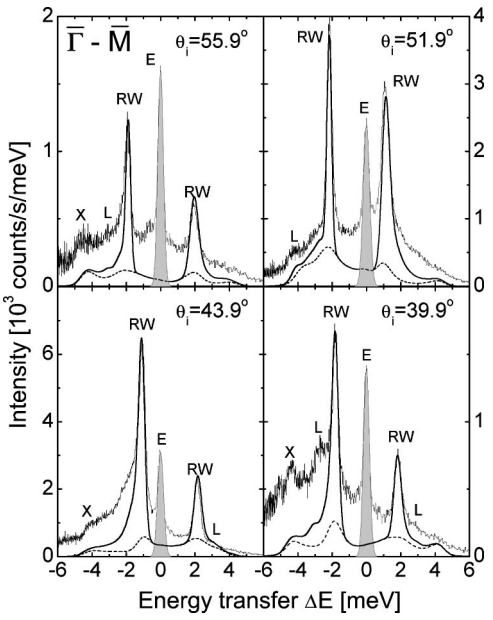

FIG. 14. Comparison of experimental (thin noisy line) and calculated EBA (thick full line) phonon excitation intensities as functions of energy transfer for in-sagittal-plane He atom scattering from Xe(111) surface along the $\bar{\Gamma}$-$\bar{M}$ direction. The four panels show spectra for the same incident energy $E_i=10.5$ meV and substrate temperature $T_s=40K$ and for four different incident angles θ_i. The incoherent elastic peak arising from imperfections in the Xe(111) surface, which does not derive from the EBA formalism outlined in Sec. V, is denoted by the shaded peak. The dashed curve denotes the calculated multiphonon background which exhibits maxima at about twice the RW frequency at the zone edge. Note that the experimental peaks denoted by *X* are not reproduced in the one-phonon calculations utilizing the dynamical matrix of a perfect Xe(111) surface.

Assessments of the effects of higher order phonon processes on the scattering spectra necessitate the full EBA calculations to be carried out. This means that also the terms beyond zeroth and first order in the series expansion of $\exp[2W^{\mathrm{EBA}}_{\mathbf{k}_i,T_s}(\boldsymbol{\mathcal{R}},\tau)]$ should be retained in the integrand on the RHS of Eq. (10). On the other hand, once the elastic and one-phonon scattering intensities have been calculated, the true multiphonon background encompassing two, three, and other higher order processes is obtained by taking the $(\tau,\boldsymbol{\mathcal{R}})$-Fourier transform of the expression $\{\exp[2W^{\mathrm{EBA}}_{\mathbf{k}_i,T_s}(\boldsymbol{\mathcal{R}},\tau)]-1-2W^{\mathrm{EBA}}_{\mathbf{k}_i,T_s}(\boldsymbol{\mathcal{R}},\tau)\}$ and multiplying it by the corresponding Debye-Waller factor $\exp[-2W^{\mathrm{EBA}}_{\mathbf{k}_i,T_s}]$. Now, the specificity of the multiphonon component of the HAS spectra in the present scattering regime is in the dominance of one- and two-phonon processes, as evidenced by the values of the Debye-Waller exponents shown in Fig. 12. In this situation the probability of two phonon scattering reaches maximum in the cases involving two RW phonons with wavevectors from the opposite edges of the first SBZ where their density of states is largest. This gives rise to maxima in the multiphonon scattering spectra at

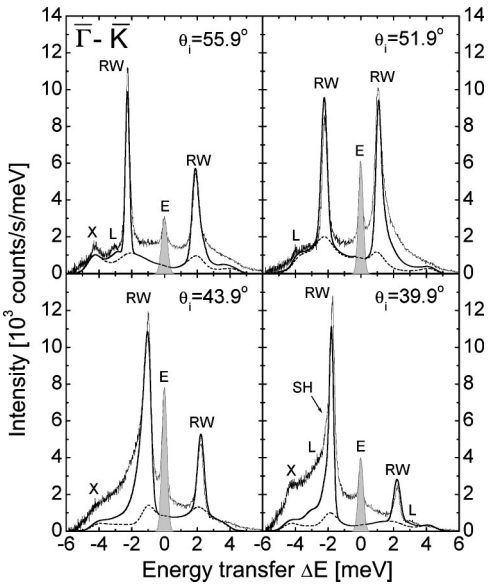

FIG. 15. Same as in Fig. 14 but along the $\bar{\Gamma}$-$\bar{K}$ direction of the surface Brillouin zone.

around ± 4.3 meV, i.e., approximately twice the RW energy at the zone edge. The thus calculated multiphonon background juxtaposed with the earlier calculated one-phonon DWBA scattering intensities will serve as a basis for our theoretical interpretations of the TOF spectra.

Figure 14 shows a comparison of four representative HAS-TOF spectra (''noisy'' thin full line) recorded at $E_i = 10.5$ meV along the $\bar{\Gamma}$-$\bar{M}$ direction with the full EBA scattering intensities (full thick lines). Since the absolute experimental inelastic intensities which depend on many factors are unknown, all calculated intensities in a particular spectrum have been scaled by a *common factor* so as that the largest calculated and measured intensities (peak areas) match each other at the largest inelastic peak. The elastic peaks in the experimental spectra at $\Delta E = 0$ due to incoherent scattering from surface defects, which are not present in the EBA calculations for an ideal surface, are indicated by gray shaded peaks. The broad multiphonon background under the single phonon peaks, which has been calculated following the procedure described in the previous paragraph, is shown by the dashed lines to facilitate comparisons of the relative intensities of the measured and calculated single phonon features.

It is gratifying that the present EBA calculations accurately reproduce the relative intensities of both the one-phonon and multiphonon loss and gain features in the TOF spectra in Fig. 14. In particular, there is a quantitative agreement between the measured and computed relative intensities of the Rayleigh phonon loss and gain peaks. Most of the other single phonon features in the TOF spectra are reproduced and hence can be identified despite the non-negligible background. The *L*-mode energy loss, which approaches 4.3 meV at the $\bar{M}$ point, is also nicely reproduced in the calculated spectra (see upper right panel in Fig. 14). The experimental loss peaks denoted by *X* at $\Delta E = -4.3$ meV with ΔK values close to the zone center can be interpreted as a feature arising from the two RW phonon exchange processes that produce ''decepton type'' of maxima in the calculated multiphonon background. For the $\bar{\Gamma}$-$\bar{K}$ azimuth similar good agreement between the measured TOF and calculated EBA HAS intensities is found for the same incident energy of 10.5 meV (Fig. 15).

The experimental and theoretical results shown in Figs. 11, 14, and 15 present strong evidence for the observation of all three expected dispersive surface phonon modes, namely, the Rayleigh wave (RW), longitudinal (L), and shear horizontal (SH) phonons. The Rayleigh phonon peaks are the most intense along all directions, as expected from their predominant Z polarization (see second panel in Fig. 11). The longitudinal mode is most clearly seen in the experimental results along the $\bar{\Gamma}$-$\bar{M}$ azimuth and weakly along the $\bar{\Gamma}$-$\bar{K}$ direction, which is also reproduced in the calculated spectra in Figs. 14 and 15. As shown in Fig. 11, the shear horizontal mode was not observed along the $\bar{\Gamma}$-$\bar{M}$ azimuth. Since this is a high symmetry direction of the surface and of the semi-infinite Xe(111) crystal one has $\mathbf{e}_\kappa(\mathbf{Q},\mathrm{SH}) \perp \mathbf{Q}$ and the SH contribution to the *Z*-polarized density of states is zero along this direction, due to which expression (15) vanishes in the first SBZ. However, the SH mode has discernible intensity in the measured spectra along the other surface symmetry direction $\bar{\Gamma}$-$\bar{K}$-$\bar{M}'$, particularly between the $\bar{K}$ and $\bar{M}'$ points. This is expected because it is not a high symmetry direction of the surface with respect to the underlying Xe layers. Here along the $\bar{\Gamma}$-$\bar{K}$ segment of the first SBZ the SH-mode acquires a fractional *Z* polarization, and along the $\bar{K}$-$\bar{M}'$ segment outside the first SBZ the exchanged parallel momentum $\Delta\mathbf{K} = \mathbf{Q} + \mathbf{G}$ is nearly parallel to the polarization vector of the SH mode. Both effects give rise to a nonvanishing scalar product in Eq. (15), and thereby to a nonvanishing coupling matrix element in Eq. (13).

Another interesting feature is the maximum in the ΔK dependence of the RW intensities shown in Figs. 5 and 8. In previous investigations of the RW intensity peaks as a function of ΔK a monotonic, nearly exponential fall-off with ΔK was observed for flat metal surfaces.[42–44] The $\Delta\mathbf{K}$ dependence of the RW phonon excitation probabilities, $P^{\mathrm{RW}}_{\mathbf{k}_i,T_s}(\Delta\mathbf{K})$, calculated within the present model are shown in insets in Figs. 5 and 8 for the experimental projectile incident energies, scattering directions and substrate temperature, but they are not in accord with the experimental trends shown in the main panel of the figures. This again signals that the present theoretical description of inelastic scattering cannot reproduce the absolute scattering intensities from nonideal surfaces for reasons that are briefly discussed below.

The variation of $P^{\mathrm{RW}}_{\mathbf{k}_i,T_s}(\Delta\mathbf{K})$ with $\Delta\mathbf{K}$, and hence with θ_i, arises from a combined effect of the $\Delta\mathbf{K}$ dependences from the phonon induced Debye-Waller factor (see Fig. 12), the DWBA scattering matrix elements (13), the Bose-Einstein distribution $\bar{n}(\hbar\omega_{\Delta\mathbf{K},\mathrm{RW}})$, and the total energy conservation condition. The thus calculated $P^{\mathrm{RW}}_{\mathbf{k}_i,T_s}(\Delta\mathbf{K})$ complies with the optical theorem for inelastic scattering from a *flat* surface

that manifests itself through the unitarity of the scattering spectrum (10). The attenuation of $P^{\mathrm{RW}}_{\mathbf{k}_i,T_s}(\Delta\mathbf{K})$ for larger $\Delta\mathbf{K}$ is controlled by the phonon-induced Debye-Waller factor and the Gaussian cutoff in the potential (14). Other factors exhibit nonuniform $\Delta\mathbf{K}$ variation over the SBZ, particularly the RW polarization vector that is associated with the topmost Xe layer [see Eq. (2) and Fig. 11]. However, the experimentally observed dependence of the RW excitation intensity cannot be described only by the $\Delta\mathbf{K}$ behavior of $P^{\mathrm{RW}}_{\mathbf{k}_i,T_s}(\Delta\mathbf{K})$ because it does not include (i.e., is not multiplied by) the ''total'' Debye-Waller factor which describes the loss of the incoming beam flux into all inelastic and off-specular elastic scattering channels open in the experiment.[47,71] Namely, in the case of corrugated surfaces and surfaces with defects an additional reduction of the inelastic scattering intensities occurs due to the scattering of initial beam flux into the diffraction and diffuse elastic scattering channels, and these processes are not accounted for within the present model based on the *flat* static atom-surface potential (8).

Thus, a rapid variation of the specular beam intensity with the change of the incident angle has been observed in HAS from monolayers of Xe on graphite,[72] and interpreted theoretically[73] as due to the diffraction and selective adsorption effects (see Figs. 3 and 9 in Ref. 73). The loss of beam flux into diffraction and diffuse elastic scattering channels will also lead to a rearrangement of the inelastic intensities as θ_i (and hence $\Delta\mathbf{K}$) is varied, and this can be described in terms of the diffraction- and the diffuse-scattering-induced Debye-Waller factors,[71] in analogy to the phonon-induced component. It is important to observe that although all three components of the total or integrated DWF depend on E_i, θ_i, and T_s, they are constant for a particular TOF spectrum in which these experimental parameters are fixed. However, as the total DWF varies in magnitude from one scattering spectrum to another as the scattering conditions are changed, it acts as a rescaling factor for the TOF intensities. Indeed, our analyses also show that the abrupt variation of the total signal intensity in the $\overline{\Gamma}$-$\overline{K}$ angular distribution at $\theta_i = 40°$ in Fig. 2 coincides with the change of the number of open off-specular diffraction channels, and the magnitude of the corresponding $\Delta\mathbf{K}$ coincides with the value around which the experimental RW intensity is maximum. Therefore, comparisons of the absolute experimental intensities of phonon loss and gain features with those calculated in the EBA for *different* TOF spectra and shown in the insets of Figs. 5 and 8 require an accurate knowledge of such total DWF, which is not possible at present. In this situation the only meaningful comparisons can be made for the relative experimental and theoretical intensities of the peaks which bear the same total Debye-Waller factor, i.e., for the peaks from the *same* TOF spectrum, as has been done in Figs. 14 and 15.

VII. CONCLUSIONS

New helium atom scattering results and theoretical calculations for the Xe(111) surface have been presented. In addition to the Rayleigh phonon mode, which had been measured previously,[3–5,7,8] evidence for the longitudinal and shear horizontal modes of the Xe(111) surface was found. The excitation of the shear horizontal mode, in particular, was only observed in the surface direction $\overline{\Gamma}$-$\overline{K}$-$\overline{M}'$ for which it is symmetry allowed along the $\overline{\Gamma}$-$\overline{K}$ segment in the first SBZ and along the $\overline{K}$-$\overline{M}'$ segment outside the first SBZ.

The theoretical model developed here can explain all of the experimental inelastic scattering intensities, including the experimentally detected dispersionless X feature at $\Delta E = -4.3$ meV near the zone center, using gas-phase He-Xe and Xe-Xe potentials without any modification. The X feature, which is resolvable in only some of the spectra, can be attributed either to vibrations associated with surface defects which were not included in the theoretical model or, as supported by the present calculations, to multiphonon ''decepton'' effects involving excitations of two RW phonons with wavevectors from the opposite edges of the first SBZ. Thus, the present work shows that there are no anomalous scattering effects for thick xenon layers, unlike the recent results for xenon monolayers adsorbed on Cu and NaCl substrates.[30–33] This calls for *ab initio* calculations of the interactions of adlayer Xe atoms with the quoted substrates as this could shed more light on the properties of intralayer force constants that represent an essential ingredient in theoretical interpretations of the phonon excitation intensities in HAS from these systems.

ACKNOWLEDGMENTS

The work in Zagreb has been supported in part by the Joint National Science Foundation Grant No. JF 133.

*Corresponding author. Email: branko@ifs.hr

†Present address: Infineon Technologies, Corporate Research, Otto-Hahn-Ring 6, D-81739 München, Germany.

[1] L.W. Bruch, M.W. Cole, and E. Zaremba, in *Physical Adsorption: Forces and Phenomena*, International Series of Monographs on Chemistry Vol. 23 (Clarendon Press, Oxford, 1997).

[2] H. Taub, K. Carneiro, J.K. Kjems, L. Passell, and J.P. McTague, Phys. Rev. B **16**, 4551 (1977).

[3] K.D. Gibson and S.J. Sibener, Phys. Rev. Lett. **55**, 1514 (1985).

[4] K.D. Gibson and S.J. Sibener, Faraday Discuss. Chem. Soc. **80**, 203 (1985).

[5] K.D. Gibson, S.J. Sibener, B.M. Hall, D.L. Mills, and J.E. Black, J. Chem. Phys. **83**, 4256 (1985).

[6] K. Kern, R. David, R.L. Palmer, and G. Comsa, Phys. Rev. Lett. **56**, 2823 (1986).

[7] K. Kern, R. David, R.L. Palmer, and G. Comsa, Surf. Sci. **175**, L669 (1986).

[8] P. Zeppenfeld, U. Becher, K. Kern, and G. Comsa, J. Electron Spectrosc. Relat. Phenom. **54**, 265 (1990).

[9] Th. Seyller, M. Caragiu, R.D. Diehl, P. Kaukasoina, and M. Lindroos, Chem. Phys. Lett. **291**, 567 (1998).

[10] Th. Seyller, M. Caragiu, R.D. Diehl, P. Kaukasoina, and M. Lindroos, Phys. Rev. B **60**, 11 084 (1999).

[11] K. Horn and A.M. Bradshaw, Solid State Commun. **30**, 545

(1979); C. Mariani, K. Horn, and A.M. Bradshaw, Phys. Rev. B **25**, 7798 (1982).
[12] K. Wandelt, J. Hulse, and J. Küppers, Surf. Sci. **104**, 212 (1981); K. Wandelt and J. Hulse, J. Chem. Phys. **80**, 1340 (1984).
[13] K. Wandelt and B. Gumhalter, Surf. Sci. **140**, 355 (1984), and references therein.
[14] T. Mandel, G. Kaindl, M. Domke, W. Fischer, and W.D. Schneider, Phys. Rev. Lett. **55**, 1638 (1985).
[15] A. Jablonski, S. Eder, K. Markert, and K. Wandelt, J. Vac. Sci. Technol. A **4**, 1510 (1986).
[16] I.T. Steinberger and K. Wandelt, Phys. Rev. Lett. **23**, 2494 (1987).
[17] T. Schmitz-Hübsch, K. Oster, J. Radnik, and K. Wandelt, Phys. Rev. Lett. **74**, 2595 (1995).
[18] M. Grüne, T. Pelzer, K. Wandelt, and I.T. Steinberger, J. Electron Spectrosc. Relat. Phenom. **98-99**, 121 (1999).
[19] M. Scheffler, K. Horn, A.M. Bradshaw, and K. Kambe, Surf. Sci. **80**, 69 (1979).
[20] M. Weinelt, P. Trischberger, W. Widdra, K. Eberle, P. Zebisch, S. Gokhale, D. Menzel, J. Henk, R. Feder, H. Dröge, and H.-P. Steinrück, Phys. Rev. B **52**, R17 048 (1995).
[21] P. Trischberger, H. Dröge, S. Gokhale, J. Henk, H.-P. Steinrück, W. Widdra, and D. Menzel, Surf. Sci. **377-379**, 155 (1997).
[22] E. Bertel, W. Jacob, and V. Dose, Appl. Phys. A: Solids Surf. **44**, 93 (1987); E. Bertel, Surf. Sci. **367**, L61 (1996), and references therein.
[23] K. Horn, K.H. Frank, J.A. Wilder, and B. Reihl, Phys. Rev. Lett. **57**, 1064 (1986); J. Vac. Sci. Technol. A **5**, 739 (1987); K.H. Frank, K. Horn, J. Wilder, and E.E. Koch, Appl. Phys. A: Solids Surf. **44**, 97 (1987).
[24] W. Widdra, P. Trischberger, W. Frieß, D. Menzel, S.H. Payne, and H.J. Kreuzer, Phys. Rev. B **57**, 4111 (1998).
[25] P. Zeppenfeld, S. Horch, and G. Comsa, Phys. Rev. Lett. **73**, 1259 (1994).
[26] W. Allers, A. Schwarz, V.D. Schwarz, and R. Wiesendanger, Europhys. Lett. **48**, 276 (1999).
[27] B.F. Mason and B.R. Williams, Surf. Sci. **148**, L686 (1984).
[28] P. Zeppenfeld, M. Büchel, R. David, G. Comsa, C. Ramseyer, and C. Girardet, Phys. Rev. B **50**, 14 667 (1994).
[29] C. Ramseyer, V. Pouthier, C. Girardet, P. Zeppenfeld, M. Büchel, V. Diercks, and G. Comsa, Phys. Rev. B **55**, 13 203 (1997).
[30] A.P. Graham, M.F. Bertino, F. Hofmann, J.P. Toennies, and Ch. Wöll, J. Chem. Phys. **106**, 6194 (1997).
[31] J. Braun, D. Fuhrmann, A. Šiber, B. Gumhalter, and Ch. Wöll, Phys. Rev. Lett. **80**, 125 (1998).
[32] A. Šiber, B. Gumhalter, J. Braun, A.P. Graham, M.F. Bertino, J.P. Toennies, D. Fuhrmann, and Ch. Wöll, Phys. Rev. B **59**, 5898 (1999).
[33] R. Gerlach, A.P. Graham, J.P. Toennies, and H. Weiss, J. Chem. Phys. **109**, 5319 (1998).
[34] L.W. Bruch, J. Chem. Phys. **107**, 4443 (1997).
[35] L.W. Bruch, A.P. Graham, and J.P. Toennies, J. Chem. Phys. **112**, 3314 (2000).
[36] R.A. Aziz and M.J. Slaman, Mol. Phys. **58**, 679 (1986); A.K. Dham, A.R. Allnatt, W.J. Meath, and R.A. Aziz, *ibid.* **67**, 1291 (1989); A.K. Dham, W.J. Meath, A.R. Allnatt, R.A. Aziz, and M.J. Slaman, Chem. Phys. **142**, 173 (1990).
[37] B.J. Palmer, D.H. Saunderson, and D.N. Batchelder, J. Phys. C **6**, L313 (1973); N.A. Lurie, G. Shirane, and J. Skalyo, Jr., Phys. Rev. B **9**, 5300 (1974); N.P. Gupta and P.K. Garg, Solid State Commun. **16**, 607 (1975).
[38] J.P. Toennies, in *Surface Phonons*, Springer Series in Surface Sciences Vol. 21, edited by W. Kress and F. de Wette (Springer-Verlag, Berlin, 1988), p. 111.
[39] A.D. Novaco and J.P. McTague, Phys. Rev. Lett. **38**, 1286 (1977).
[40] T. Engel and K.H. Rieder, in *Structural Studies of Surface with Atomic and Molecular Beams*, Springer Tracts in Modern Physics No. 91 (Springer, Berlin, 1982), p. 55.
[41] D. Farias and K.H. Rieder, Rep. Prog. Phys. **61**, 1575 (1998).
[42] D. Eichenauer, U. Harten, J.P. Toennies, and V. Celli, J. Chem. Phys. **86**, 3693 (1987).
[43] F. Hofmann, J.P. Toennies, and J.R. Manson, J. Chem. Phys. **101**, 10 155 (1994).
[44] G. Witte, J.P. Toennies, and Ch. Wöll, Surf. Sci. **323**, 228 (1995).
[45] R. Allen, G.P. Alldredge, and F.W. de Wette, Phys. Rev. B **4**, 1648 (1971); **4**, 1661 (1971); **4**, 1682 (1971).
[46] L.W. Bruch, A.P. Graham, and J.P. Toennies, Mol. Phys. **95**, 579 (1998).
[47] A. Bilić and B. Gumhalter, Phys. Rev. B **52**, 12 307 (1995).
[48] K.T. Tang and J.P. Toennies, J. Chem. Phys. **66**, 1496 (1977); Z. Phys. D: At., Mol. Clusters **1**, 91 (1986).
[49] K.M. Smith, A.M. Rulis, G. Scoles, R.A. Aziz, and V. Nain, J. Chem. Phys. **67**, 152 (1977).
[50] A.F. Devonshire, Proc. R. Soc. London, Ser. A **158**, 269 (1937).
[51] V. Bortolani and A.C. Levi, Riv. Nuovo Cimento **9**, 1 (1986).
[52] V. Celli, in *Surface Phonons*, edited by W. Kress and F.W. de Wette (Springer, Berlin, 1991), p. 167.
[53] G. Santoro and V. Bortolani, in *Inelastic Energy Transfer in Interactions with Surfaces and Adsorbates*, edited by B. Gumhalter, A.C. Levi, and F. Flores (World Scientific, Singapore, 1993), p. 1.
[54] E. Kirsten and K.H. Rieder, Surf. Sci. **222**, L837 (1989); E. Kirsten, G. Parschau, and K.H. Rieder, *ibid.* **236**, L365 (1990).
[55] B. Gumhalter, A. Šiber, and J.P. Toennies, Phys. Rev. Lett. **83**, 1375 (1999).
[56] K. Burke, B. Gumhalter, and D.C. Langreth, Phys. Rev. B **47**, 12 852 (1993).
[57] B. Gumhalter, K. Burke, and D.C. Langreth, Surf. Rev. Lett. **1**, 133 (1994).
[58] W. Brenig, Z. Phys. B **36**, 81 (1979).
[59] B. Gumhalter and A. Bilić, Surf. Sci. **370**, 47 (1997).
[60] B. Gumhalter, Surf. Sci. **347**, 237 (1996).
[61] A. Šiber and B. Gumhalter, Surf. Sci. **385**, 270 (1997).
[62] V. Bortolani, A. Franchini, N. Garcia, F. Nizzoli, and G. Santoro, Phys. Rev. B **28**, 7358 (1983).
[63] V. Celli, G. Benedek, U. Harten, J.P. Toennies, R.B. Doak, and V. Bortolani, Surf. Sci. **143**, L376 (1984).
[64] A. Glebov, J.R. Manson, J.G. Skofronick, and J.P. Toennies, Phys. Rev. Lett. **78**, 1508 (1997).
[65] A.M. Lahee, J.R. Manson, J.P. Toennies, and Ch. Wöll, J. Chem. Phys. **86**, 7194 (1987).
[66] D. Evans, V. Celli, G. Benedek, J.P. Toennies, and R.B. Doak, Phys. Rev. Lett. **50**, 1854 (1983).
[67] G. Benedek, Phys. Rev. Lett. **35**, 234 (1975).
[68] S. Miret-Artés, Surf. Sci. Lett. **366**, L735 (1996); G. Benedek, R. Gerlach, A. Glebov, G. Lange, S. Miret-Artes, J.G. Skofronick, and J.P. Toennies, Phys. Rev. B **53**, 11 211 (1996).

[69] R.B. Doak, in *Atomic and Molecular Beam Methods*, Vol. 2, edited by G. Scoles (Oxford University Press, New York, 1992), p. 384.

[70] The calculations yield frequencies of 0.95 meV for the parallel, and 1.65 and 2.7 meV for perpendicular vibrations of isolated xenon atoms at the center ($\overline{\Gamma}$) of the backfolded first SBZ.

[71] B. Gumhalter and D.C. Langreth, Phys. Rev. B **60**, 2789 (1999).

[72] G. Bracco, MS thesis, University of Genova, 1981.

[73] J.M. Hutson and C. Schwartz, J. Chem. Phys. **79**, 5179 (1983).